



Cite this: *Energy Environ. Sci.*, 2023, 16, 6110

In situ polymerization of 1,3-dioxane as a highly compatible polymer electrolyte to enable the stable operation of 4.5 V Li-metal batteries†

Yang Liu,^{‡,a} Hanqin Zou,^{‡,a} Zili Huang,^a Qiuxia Wen,^a Jiawei Lai,^a Yuping Zhang,^a Jinghao Li,^{*,b} Kui Ding,^{*,a} Jian Wang,^c Ya-Qian Lan^a and Qifeng Zheng^{ID, *,a}

1,3-Dioxolane (DOL) has received great attention as a polymer electrolyte (PE) for Li-metal batteries (LMBs) due to its desirable interfacial contact and decent compatibility with Li-metal, yet it suffers from poor oxidation stability, thus making it inadequate for high-voltage cathodes. Herein, by tuning the molecular structure of the liquid precursor from being a five-membered cyclic DOL to a six-membered cyclic 1,3-dioxane (DOX), the *in situ* fabricated poly(DOX) PE obtained exhibits superior oxidation stability (exceeding 4.7 V) owing to its prolonged alky chain that lowers its HOMO level. Moreover, the prolonged alky chain also weakens its solvating ability, which not only affords a high Li⁺ transference number (0.75), but also contributes to a highly robust and conductive inorganic-rich solid–electrolyte interphase, bestowing highly dense Li deposition morphology as well as excellent Li plating/stripping reversibility for over 1300 h. As a result, this newly developed poly(DOX) PE delivers outstanding cycling stability for diversified high-voltage cathodes including but not limited to LiNi_{0.33}Co_{0.33}Mn_{0.33}O₂, LiNi_{0.8}Co_{0.1}Mn_{0.1}O₂, and LiCoO₂ under a high cut-off voltage of 4.5 V, paving the way for the practical application of high-voltage high-energy-density solid-state batteries.

Received 23rd August 2023,
Accepted 1st November 2023

DOI: 10.1039/d3ee02797j

rsc.li/ees

Broader context

The urgent need for high-energy and high-safety batteries is leading to extensive research studies in solid-state Li-metal batteries (LMBs). Among the various solid-state electrolytes, polymer electrolytes (PEs) are considered to be particularly promising owing to their high flexibility, excellent processability, lightweight, and low cost. However, low ionic conductivity and high interfacial resistance of PEs remain the main challenges for their practical application. Construction of PEs by *in situ* polymerization of liquid precursors would circumvent these challenges. 1,3-Dioxolane, which undergoes cationic ring-opening polymerization to form a polyether-based PE, has achieved high-levels of success, yet it suffers from poor oxidation stability. In this work, we successfully develop an *in situ* polymerized 1,3-dioxane PE with superior oxidation stability and elevated Li-metal compatibility, which enables the stable operation of LMBs with various state-of-the-art high-voltage cathodes (4.5 V). Coupled with its high adaptability to the current battery manufacturing system, this work holds great universality and potential for practical industrialization, which represents a significant advancement in the development of highly compatible PEs for safe batteries with high-energy density.

Introduction

The rapidly increasing demand of electric vehicles and energy storage grids is pushing the current lithium-ion battery (LIB) technology with regard to their energy density limit.^{1–4} To upgrade the energy density of batteries, theoretically, employing a Li-metal anode and high-voltage cathodes (4.0 V-above class) has been considered as one of the most effective pathways.^{5,6} However, the conventional organic liquid electrolytes continuously react with both Li-metal anodes and high-voltage cathodes, depleting the electrolytes and thickening the electrode/electrolyte interphases.^{7–9} Especially for the Li-metal anode side, the inhomogeneous deposition of Li⁺ in organic liquid electrolytes would result

^a School of Chemistry, South China Normal University, 55 West Zhongshan Rd., Guangzhou 510631, China. E-mail: dingkui366@m.scnu.edu.cn, qifeng.zheng@m.scnu.edu.cn

^b Department of Energy, Environmental, and Chemical Engineering, Washington University in St. Louis, 1 Brookings Dr, St. Louis, MO 63130, USA. E-mail: jinghao@wustl.edu

^c School of Energy and Environment, City University of Hong Kong, Kowloon, Hong Kong SAR, China

† Electronic supplementary information (ESI) available. See DOI: <https://doi.org/10.1039/d3ee02797j>

‡ These authors contributed equally.

in uncontrollable dendritic growth and formation of dead lithium, leading to low Coulombic efficiency (CE), poor cycle life, and even short-circuiting.^{10,11} Moreover, the highly volatile and flammable characteristics of organic liquid electrolytes would exacerbate the safety hazards of Li-metal batteries (LMBs).^{12,13}

Tremendous efforts have been devoted to circumvent these challenges, among which solid-state electrolytes (SSEs) are considered to be particularly promising owing to their intrinsic characteristics of good chemical stability, high mechanical strength and flame retardancy.^{14,15} As a result, the utilization of SSEs is demonstrated to effectively inhibit the parasitic reaction with Li-metal, restrain the growth of lithium dendrites, and resolve the safety issues associated with organic liquid electrolyte (*e.g.*, leakage and flammability).¹⁶ However, the poor interfacial contact between SSEs and electrodes will greatly push up the internal resistance, which has prevented the practical application of solid-state LMBs.¹⁷ To achieve intimate interfacial contact, an *in situ* polymerization technique was recently developed, where a liquid precursor (*i.e.*, monomer) was injected into cells during assembly, just like traditional liquid batteries.^{18,19} Since the liquid precursor has low viscosity and good wettability as traditional liquid electrolytes, it can easily penetrate into the electrodes.^{20,21} The subsequent *in situ* polymerization of the liquid precursor transforms the liquid electrolyte into polymer electrolyte (PE) with superior interfacial contact and full access to the active materials (Fig. 1a), upon which the cell using *in situ* PEs exhibits a much lower internal resistance than that using *ex situ* PEs (*i.e.*, conventional pre-manufactured PEs).

Therefore, various liquid solvent precursors, such as vinylene carbonate (VC),²² fluoroethylene carbonate (FEC),²³ 1,3-dioxolane

(DOL),²⁴ and tetrahydrofuran (THF),²⁵ have been investigated to form PEs in the cells *via in situ* polymerization. Among these, the *in situ* polyether-based PEs have attracted intensive research attentions in recent years owing to their good compatibility towards Li-metal anodes. Represented by DOL monomer that undergoes cationic ring-opening polymerization in the presence of Lewis acid, such as lithium hexafluorophosphate (LiPF₆) and aluminum trifluoromethanesulfonate [Al(OTf)₃], has achieved high-levels of success.^{18,19,26} The resulting poly-DOL (P-DOL) PEs have demonstrated high ionic conductivity, good Li plating/stripping reversibility, and stable cycling when matched with low-voltage cathodes of LiFeO₄ (LFP).^{18,19,27,28} However, the P-DOL chain decomposes easily at high-voltage which has been confirmed lately (Fig. 1b), exhibiting poor electrochemical performance with high-voltage cathodes (4 V-above class).^{19,29} Therefore, it is highly necessary to search for other alternative liquid precursors that can be *in situ* polymerized to form polyether-based PEs with high-voltage tolerance.

In this work, we for the first time report the *in situ* polymerization of the 1,3-dioxane (DOX) monomer as novel PE with superior oxidation stability and excellent Li compatibility. As shown in Fig. 1c, the DOX molecule is a six-membered ring ether, thereby the *in situ* polymerized poly-DOX (P-DOX) has a longer alkyl chain than that of P-DOL, which could lower its highest occupied molecular orbital (HOMO) and thereby increase its oxidative stability. Furthermore, increasing the alkyl chain is demonstrated to reduce the solvation ability of the P-DOX, which leads to anion-derived inorganic-rich solid-electrolyte interphase (SEI) formation that largely improves the interfacial compatibility between Li-metal and P-DOX PE. The synthesis, and thermal, physicochemical, and electrochemical

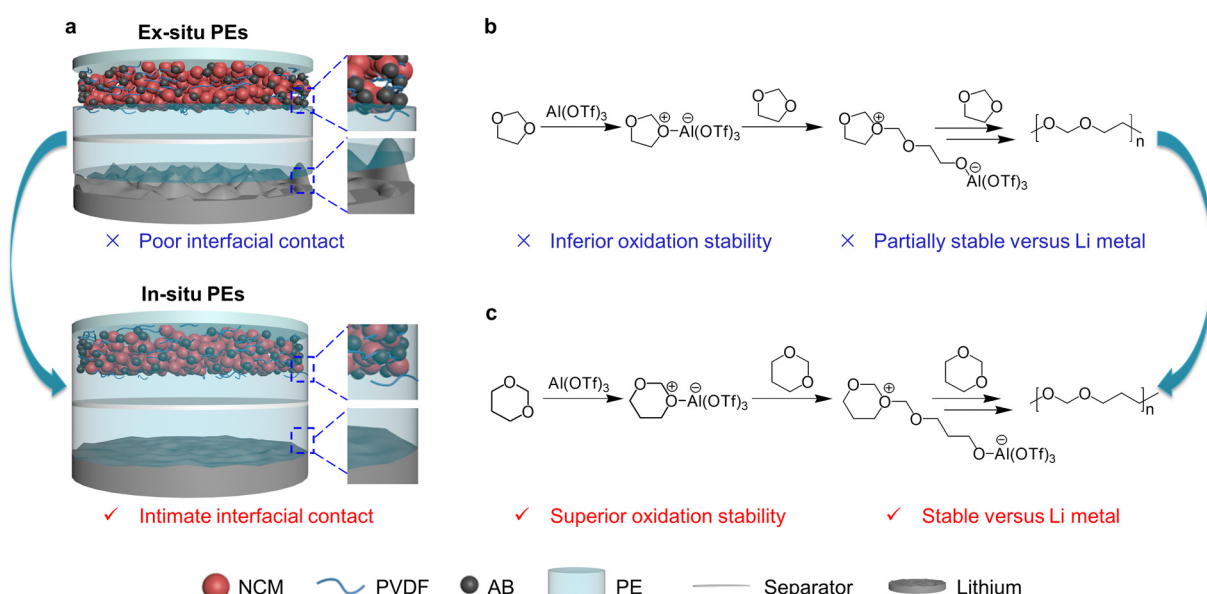


Fig. 1 Design rationale for *in situ* fabrication of high-voltage PEs. (a) Schematic illustrating the *ex situ* and *in situ* fabricated PEs. For the *in situ* fabrication of the PEs, the liquid precursor can easily penetrate into all cell components, which creates intimate interfacial contact after the subsequent *in situ* polymerization. The reaction mechanism of (b) DOL and (c) DOX initiated by Al(OTf)₃. Compared to the widely investigated P-DOL PEs, the P-DOX PE proposed in this study is expected to exhibit superior oxidation stability owing to its prolonged alkyl chain that lowers its HOMO level, and excellent Li compatibility owing to its weak solvating ability that leads to highly robust inorganic-rich SEI.

properties of the P-DOX PEs were carefully examined, showing universality and great prospects for application in high-voltage high-energy-density LMBs.

Results and discussion

Design rationale and fabrication of P-DOX PEs

As shown in Fig. 1, compared to *ex situ* polymerized PEs, the *in situ* polymerization can greatly improve interfacial contact between PEs and electrodes since the liquid electrolyte precursor is able to fully wet the electrode layers, providing connection pathways for fast ion transport. Although *in situ* polymerization of the DOL monomer has made significant progress in improving interfacial contact and cycling life of low-voltage Li||LFP cells, high-voltage tolerance and interfacial stability are still challenging.^{23,30–32} To be specific, the poor oxidative stability of the DOL solvent has prevented the resulting P-DOL PEs from being applied as high-voltage cathodes, and their compatibility with Li-metal remains to be improved.

Aiming to fabricate a novel PE *in situ* with excellent high-voltage tolerance and interfacial compatibility, the conventional five-membered DOL was replaced with a six-membered ring ether, namely DOX, owing to the following several merits: (1) the P-DOX with a longer alkyl chain has a lower HOMO energy level, which is expected to exhibit a higher oxidation stability; (2) the longer alkyl chain would also weaken the solvating ability of the P-DOX, which may not only bestow a higher Li⁺ transference number, but also lead to an inorganic-rich SEI that is more conductive and robust.

A typical cationic initiator of Al(OTf)₃ was selected to initiate the ring-opening polymerization of DOX. As shown in Fig. 2a, with the addition of an optimized Al(OTf)₃ amount of 20 mmol (Fig. S1, ESI†), the liquid electrolyte of LiFSI–DOX (molar ratio of 1 : 8) quickly polymerized without liquidity. The change of ionic conductivity *versus* time was carefully investigated to evaluate the polymerization reaction and ion transport properties of the PEs. As shown in Fig. 2b, the conductivity of the LiFSI–DOX solution with Al(OTf)₃ decreases gradually from 5.3 mS cm⁻¹ to a constant value of 0.17 mS cm⁻¹ (25 °C) after about 36 h, implying the completion of the polymerization. The corresponding electrochemical impedance spectra with the increasing polymerization time are collected in Fig. S2a (ESI†). Without Al(OTf)₃, the ionic conductivity of the LiFSI–DOX solution does not show obvious change (Fig. 2b and Fig. S2b, ESI†). For comparison purpose, the P-DOL PE was also fabricated *via* *in situ* polymerization of LiFSI–DOL solution with same salt-to-solvent molar ratio (*i.e.*, 1 : 8) under the same polymerization conditions for 12 h (Fig. S3, ESI†).

The chemical structure evolution before and after polymerization was first characterized by Fourier transform infrared spectroscopy (FTIR). As shown in Fig. 2c, the peaks of DOX ring C–O–C bond vibration almost disappear while a new peak corresponding to the long-chain C–O–C bond vibration appears after the polymerization reaction, indicating that the DOX monomer undergoes ring-opening polymerization reaction to form P-DOX. A similar phenomenon was also observed in the polymerization of DOL (Fig. S4, ESI†). ¹H nuclear magnetic resonance (NMR) further confirms their structure evolution with very high conversion rates (Fig. S5, ESI†). The molecular

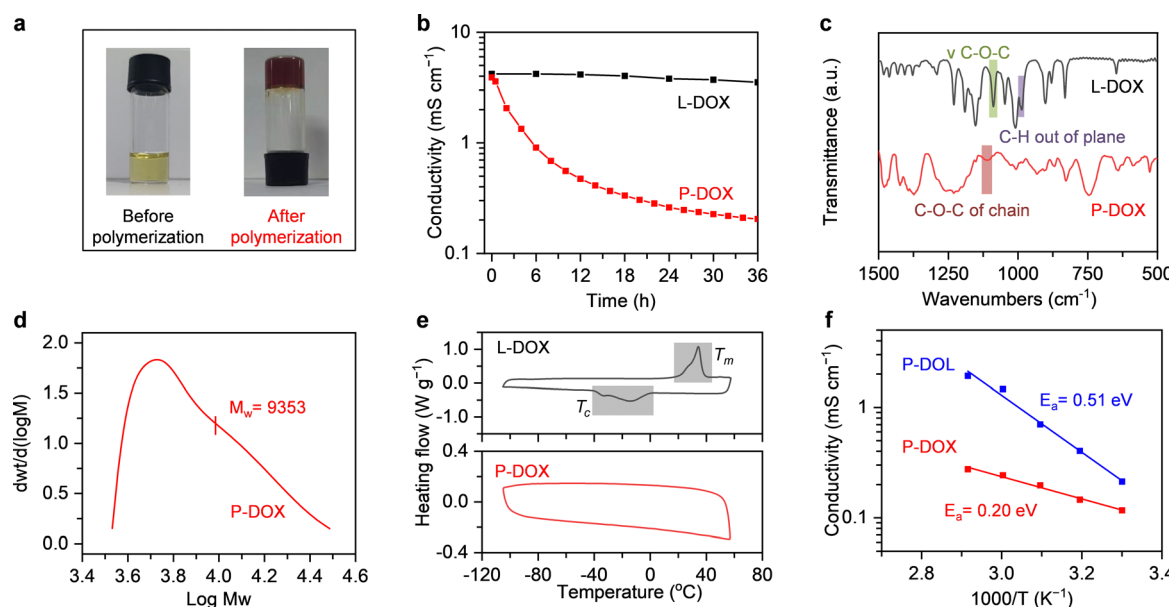


Fig. 2 Physicochemical properties of the *in situ* fabricated P-DOX PE. (a) Digital photographs of the L-DOX liquid electrolyte (1.47 M LiFSI/DOX, left) and P-DOX PE (right) formed in the liquid electrolyte containing 20 mM Al(OTf)₃ salt. (b) D.C. conductivity *versus* polymerization time for the P-DOX PE. (c) FTIR spectra of the L-DOX liquid electrolyte and P-DOX PE. (d) GPC analysis of P-DOX PE. (e) DSC curves of L-DOX liquid electrolyte (top) and P-DOX PE (bottom), of which the shaded areas indicate the melting peak (T_m) and crystallization peak (T_c), respectively. (f) Temperature-dependent ionic conductivities of the electrolytes and their fitting with Arrhenius models.

weight distribution of the resulting polymers was characterized by gel permeation chromatography (GPC) analysis, among which *ex situ* polymerized P-DOX and P-DOL exhibit weight-average molecular weights (M_w) of ~9.4 k and 57 k, respectively (Fig. 2d and Fig. S6, Table S1, ESI[†]). To better reflect the actual situation inside the cell, **NMR and GPC characterization studies were also performed with the *in situ* polymerized P-DOX and P-DOL in cells**, which showed similar results (Fig. S5 and S6, ESI[†]).

The thermal stability and crystallinity of a polymer have a significant impact on its application as SSEs. Differential scanning calorimetry (DSC) was conducted to study the thermal transitions of these electrolytes. As shown in Fig. 2e and Fig. S7 (ESI[†]), typical crystallization (T_c) and melting (T_m) phase transition peaks are observed for L-DOL and L-DOX electrolytes. However, **no crystallization peak is observed for P-DOL and P-DOX PEs, indicating that they are essentially amorphous**. According to the Li^+ conduction mechanism in polymers, the absence of a crystallization region in the *in situ* formed PEs would be beneficial for the fast migration of Li^+ , leading to high ionic conductivity.³³ In addition, the thermogravimetric analysis (TGA) reveals that the thermal stabilities of the electrolytes are significantly improved after polymerization (Fig. S8, ESI[†]). Furthermore, the flammability tests indicate that the polymerized electrolytes have much better flame retardancy than liquid electrolytes, among which the P-DOX PE did not catch fire at all (Fig. S9, ESI[†]). As shown in Fig. 2f, even though the P-DOX PE exhibits a slightly lower ionic conductivity than that of P-DOL PE at the measured temperature range from 30 to 70 °C, it delivers **a much lower activation energy (0.20 eV)** compared to P-DOL PEs (0.51 eV) according to the Arrhenius equation, which can be attributed to the **low binding energy of the P-DOX chain with Li^+** (Fig. S10, ESI[†]), showcasing that the P-DOX PE has a low Li^+ migration barrier. Furthermore, it is found that the ${}^7\text{Li}$ -NMR peak of P-DOX PE was **down shifted** compared to that of P-DOL PE, owing to the enhanced shielding effect from the nearest neighbors of Li^+ , which indicates that P-DOX has **a weaker solvating ability than P-DOL** (Fig. S11a, ESI[†]).³⁴ Moreover, as shown in Fig. S11b (ESI[†]), the Raman spectra show that the coordination state of the FSI^- anion in P-DOX shifted to a higher wavenumber compared to that in P-DOL, suggesting that the $\text{Li}^+ - \text{FSI}^-$ association was intensified in P-DOX that leads to the formation of aggregated ion pairs, which raises the reduction potential of FSI^- and thereby promotes its reductive decomposition to produce FSI^- anion-derived inorganic-rich SEI.³⁵ In addition, this peculiar ion-paired structure formed in the P-DOX PE would restrict the transport of FSI^- anions, thereby increasing the Li^+ transference number to 0.75 (Fig. S12, ESI[†]).³⁶

Superior compatibility towards high-voltage and Li-metal

The oxidation stability of the PEs is essential for their application in high-voltage high-energy density batteries. Density functional theory (DFT) calculations were first conducted to verify the oxidation stability of the P-DOL and P-DOX polymers. As shown in Fig. 3a and Fig. S13 (ESI[†]), no matter how many repeating units calculated, the P-DOX always exhibits a lower

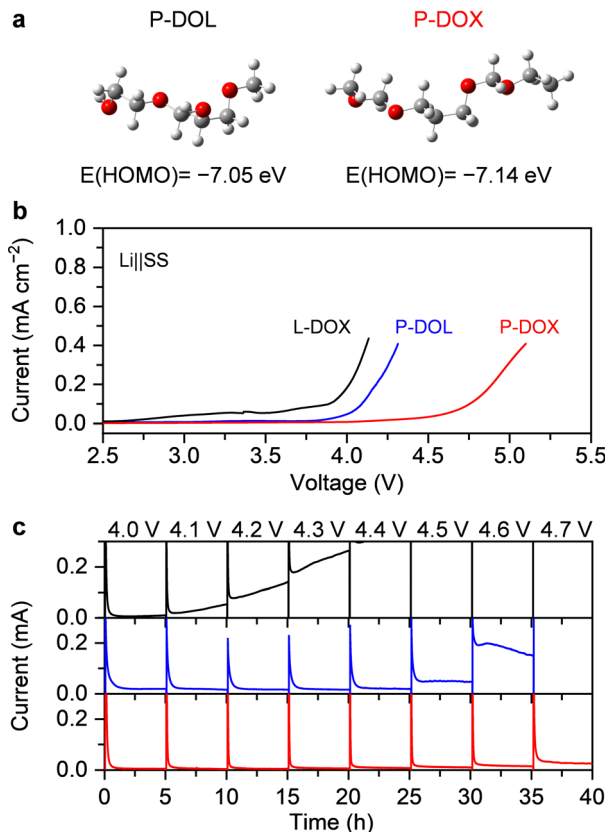


Fig. 3 High-voltage stability of the *in situ* fabricated P-DOX PE. (a) The HOMO energies of P-DOL and P-DOX polymer chains. (b) Linear sweep voltammetry (LSV) of the electrolytes at a scan rate of 1 mV s⁻¹ with stainless steel as working electrode. (c) Electrochemical floating test of the electrolytes using a NCM111 cathode.

HOMO energy level than that of P-DOL at the same chain length, suggesting an excellent oxidation stability of P-DOX. The intrinsic oxidative stability of the L-DOX, P-DOL and P-DOX electrolytes was then tested by linear sweep voltammetry (LSV) with a stainless steel (SS) as the working electrode. As shown in Fig. 3b, the oxidative decomposition of the L-DOX electrolyte occurs at around 3.5 V defined at 0.05 mA cm⁻², whereas the oxidation potential of P-DOX PE is significantly increased to **4.7 V** after *in situ* ring opening polymerization, making it suitable to match with high-voltage cathodes. The oxidation stability is also much better than that of the widely investigated **P-DOL PEs (i.e., 4.1 V)**, indicating that the oxidation stability of the PEs can be effectively improved through tuning the molecular structure of the monomer precursor. Changing the working electrode to Al foil (a common current collector for the cathode) also exhibits a similar phenomenon, that is, the P-DOX PE possesses a much higher oxidation potential than that of L-DOX and P-DOL electrolytes (Fig. S14, ESI[†]).

To further characterize the practical oxidation stability of P-DOX PE in batteries, the electrochemical floating experiment was carried out on a $\text{LiNi}_{0.33}\text{Co}_{0.33}\text{Mn}_{0.33}\text{O}_2$ (NCM111) electrode,¹⁹ where the measured leakage current provides a direct standard for evaluating the oxidation stability of electrolytes. As shown in

Fig. 3c, sharp increase in the leakage current was observed for L-DOX liquid electrolyte when elevating the voltage to 4.1 V, indicating that the liquid electrolyte is vulnerable to the oxidation. A leakage current of 22 μ A is detected for P-DOL PE at 4.0 V, and the leakage current sharply increases to that exceeding 200 μ A at 4.6 V, suggesting that the P-DOL PE is unstable under high-voltage. In sharp contrast, the leakage current remains very low for P-DOX PE even at a high voltage of 4.6 V (<20 μ A), demonstrating its superior compatibility towards high-voltage cathodes. This electrochemical floating experiment once again demonstrates that the oxidation stability of the *in situ* PEs can be effectively enhanced by tuning the molecular structure of the cyclic ether monomer.

The compatibility of PEs with Li-metal anode is another key factor affecting the performance of high-energy density LMBs. The reversibility of Li deposition and stripping processes in L-DOX, P-DOL, and P-DOX electrolytes was first investigated in Li||Li symmetric cells. For the testing at 1 mA cm^{-2} with 1 mA h cm^{-2} (Fig. 4a), all three electrolytes exhibit smooth and

low overpotential during the initial 200 h. While turbulent plating/stripping profile was observed for the symmetric cell using L-DOX liquid electrolyte later on, and a hard short-circuit occurs after 350 h, which can be ascribed to the random growth of the Li dendrites in the liquid electrolyte. Meanwhile, the overpotential was gradually increased for the P-DOL PE due to the accumulation of thick SEI and dead Li, and the cell is eventually subjected to a sudden short-circuit at about 440 h. Remarkably, using P-DOX PE, the cell demonstrates extremely stable cycling with negligible increase in the overpotential for over 1300 h. In addition, the interfacial resistance of the Li||Li symmetric cell using P-DOX PE remains very low and stable during cycling, while that using P-DOL PE or L-DOX liquid electrolyte gradually increases (Fig. S15, ESI†). The superior Li compatibility possessed by P-DOX PE may be attributed to the following two reasons: (1) the Li⁺ transference numbers of P-DOX PE (0.75) is higher than that of L-DOX electrolyte (0.19) and P-DOL PE (0.65) (Fig. S12, ESI†), which can reduce the Li⁺ concentration gradient near the Li-metal anode and thereby

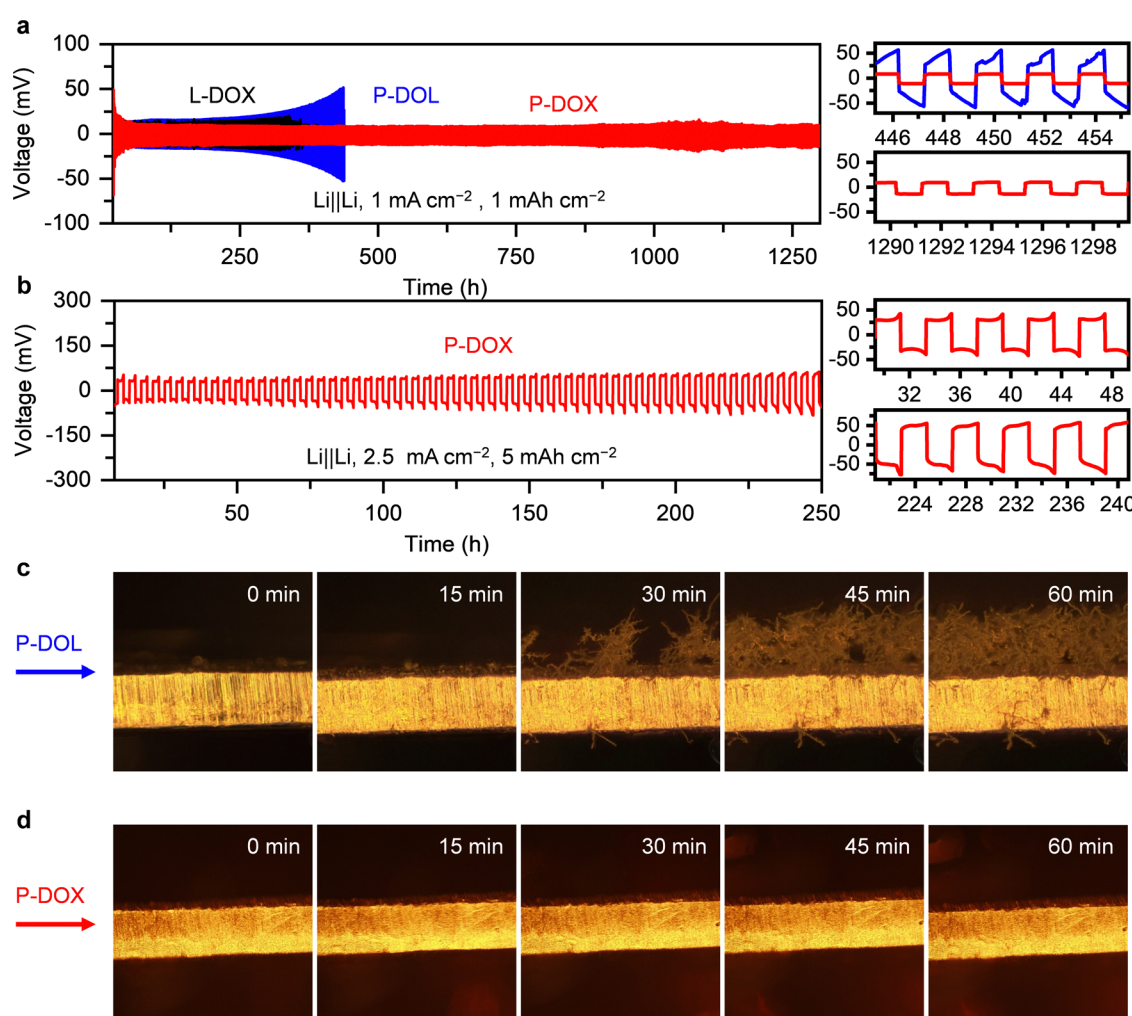


Fig. 4 Li metal compatibility in the *in situ* fabricated PE. Long-term cycling of Li||Li symmetric cells using different electrolytes at (a) 1 mA cm^{-2} for 1 mA h cm^{-2} , and (b) 2.5 mA cm^{-2} for 5 mA h cm^{-2} . The insets show the zoomed-in voltage profiles during different stages. In operando observation of the morphological evolution of electrodeposited Li under a current density of 1.0 mA cm^{-2} with (c) P-DOL and (d) P-DOX PEs.

impede the nucleation of Li dendrites, and (2) the weakened solvation ability of P-DOX alky chain with Li^+ promotes the anion-derived inorganic-rich SEI, which is more conductive and robust, which largely improves the interfacial compatibility (discussed in detail below).

When the current density was increased to 2.5 mA cm^{-2} and 3 mA cm^{-2} (Fig. 4b and Fig. S16, ESI[†]), the Li||Li cell using either L-DOX electrolyte or P-DOL PE is not able to cycle normally and the cell fails within a few cycles, while that using P-DOX PE can sustain stable cycling for hundreds of cycles. Critical current density (CCD) is an important parameter for evaluating the tolerance of batteries under high power density, which was investigated by testing Li||Li symmetric cell at progressively different current densities.³⁷ As shown in Fig. S17 (ESI[†]), when the current density increases to 5.5 mA cm^{-2} , the P-DOL PE cannot maintain a stable polarization profile with some sharp peaks appears, accompanied by a decrease in the polarization voltage caused by micro short-circuit, suggesting that the P-DOL PE has reached the CCD at this current density. In contrast, the P-DOX PE can still retain a relatively stable voltage polarization up to 8.0 mA cm^{-2} , indicating that P-DOX PE possesses better capability for withstanding high current density than P-DOL PE in the LMBs.

Li deposition morphology and interfacial chemistry

The morphology of the Li-metal electrode in a Li||Li cell after 200 cycles was characterized by using a scanning electron microscope (SEM). As shown in Fig. S18 (ESI[†]), the Li-metal electrode in a liquid L-DOX electrolyte exhibits a porous and heterogeneous morphology, which increases the interfacial resistance and leads to rapid cell failure during repeated plating/stripping processes. For the Li-metal in P-DOL PE, massive porous Li deposits disappears while the surface is still rough, owing to the fact that PE could effectively reduce the reactivity with Li-metal. In contrast, the Li-metal in P-DOX PE presents a smooth and flat surface, indicating that a highly uniform and dense Li deposition was achieved in this PE.

To intuitively observe the Li deposition behavior, the morphology of Li electrodeposits at a plating current density of 1.0 mA cm^{-2} was also observed by *in operando* optical microscopy. For a Li||Li symmetric cell with P-DOL PE, a large number of mossy and needle-like Li dendrites were observed after 30 min of deposition and continued to grow during the following plating process (Fig. 4c), indicating the insufficient Li compatibility of P-DOL PE. In sharp contrast, the Li-metal with P-DOX PE delivered a dendrite-free and smooth growth throughout the 60 min of deposition process (Fig. 4d), confirming that the rationally selected DOX monomer could bestow the resulting *in situ* polymerized PE with uniform Li deposition morphology and highly reversible Li plating/stripping behavior.

Interfacial chemistry is critical for achieving uniform Li deposition morphology, which was investigated by performing X-ray photoelectron spectroscopy (XPS) analysis using an Ar^+ sputtering technique on the Li-metal electrode after plating/stripping for 200 cycles. As shown in Fig. 5, massive organic species (mainly lithium alkoxy) were observed on the surface of Li-metal electrode in P-DOL PE, which were mainly derived from DOL or P-DOL that is considered to be unstable and resistive. Meanwhile, some inorganic species (mainly LiF and oxysulfides) were derived from the LiFSI, while their intensities significantly reduced as Ar^+ sputtering time increased. In contrast, for the Li-metal electrode in P-DOX PE, the surface is enriched with inorganic species (*i.e.*, LiF and oxysulfides), and a small amount of organic species. As Ar^+ sputtering proceeds, the inorganic species are gradually further boosted, and their intensities remain quite strong even after 150 s of sputtering, suggesting that P-DOX PE has induced the formation of more anion-derived inorganic-rich SEI compared to that of P-DOL PE, which was ascribed to the weaker Li^+ binding energy with P-DOX than P-DOL according to the DFT calculation, and NMR and Raman characterization studies (Fig. S10 and S11, ESI[†]). As well demonstrated, this inorganic-rich SEI is more stable, conductive, and beneficial for realizing highly reversible Li plating/stripping.³⁸

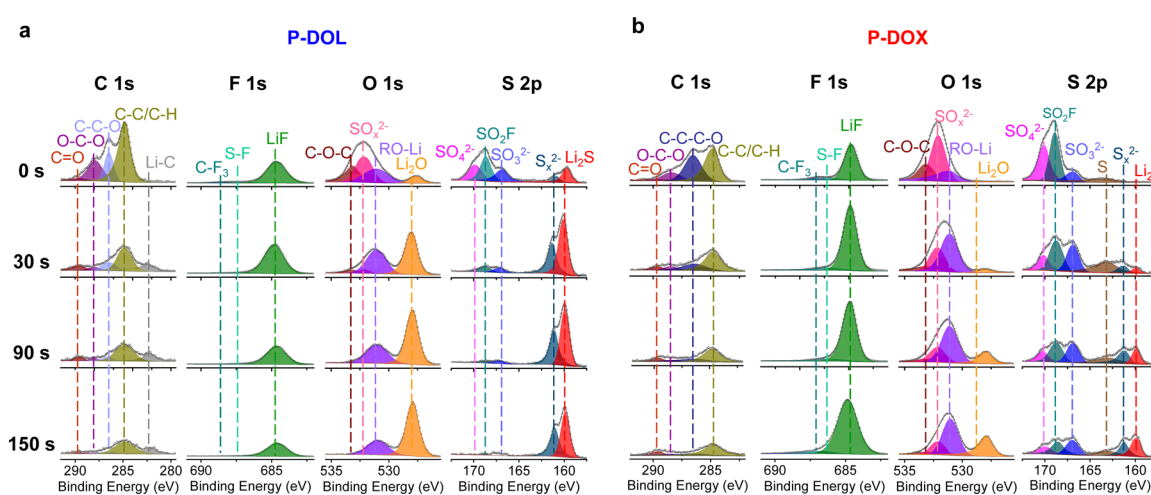


Fig. 5 Characterization of the SEI on the Li electrode. XPS depth profiles of the Li-metal electrode in (a) P-DOL and (b) P-DOX PEs at a current density of 1 mA cm^{-2} with a capacity of 1 mAh cm^{-2} after 200 plating/stripping cycles.

Stable operation of high-voltage Li-metal full cells

Having confirmed the excellent high-voltage tolerance and Li compatibility, the *in situ* polymerized P-DOX PE was eventually tested in practical LMBs with various state-of-the-art high-voltage cathodes, including NCM111, $\text{LiNi}_{0.8}\text{Co}_{0.1}\text{Mn}_{0.1}\text{O}_2$ (NCM811), and LiCoO_2 (LCO). The electrochemical performance of $\text{Li}||\text{NCM111}$ cells was first investigated with a cutoff voltage of 2.8–4.3 V. As shown in Fig. 6a, for the cell using L-DOX electrolyte or P-DOL PE, the specific capacity decreases rapidly with highly fluctuating CE, which is due to the poor oxidation tolerance of the L-DOX electrolyte and P-DOL PE as well as the formation of dendritic and dead Li at the anode side. In sharp contrast, the $\text{Li}||\text{NCM111}$ cell using P-DOX PE delivers an initial capacity of $153.2 \text{ mA h g}^{-1}$ and can still maintain a high capacity of $146.3 \text{ mA h g}^{-1}$ after 500 cycles at 0.5C, corresponding to a high-capacity retention of 95.5%, which is also much better than those reported P-DOL-based PE even with various functional solvent/additives (Table S2, ESI[†]). Furthermore, no obvious voltage polarization is shown for the cell using P-DOX PE according to their charge–discharge profiles shown in Fig. 6b. Besides, their interfacial resistance remains stable during cycling (Fig. S19b, ESI[†]), suggesting excellent interfacial compatibility towards both high voltage cathodes and Li-metal anodes while severe increase in voltage polarization and interfacial resistance can be observed for the cell using P-DOL PE (Fig. S19 and S20, ESI[†]).

The morphology of the NCM111 cathode after 500 cycles was characterized by SEM. As shown in Fig. 6c and Fig. S21 (ESI[†]), severe particle cracking and even pulverization is found for the NCM111 cathode after cycling in the L-DOX electrolyte or P-DOL PE, which is due to the severe oxidation of the L-DOX electrolyte and P-DOL PE on the surface of the cathode, causing structural degradation of the cathode. In contrast, the NCM111 cathode after cycling in P-DOX PE maintains a spherical and

intact microstructure with negligible change compared to the pristine NCM111 cathode before cycling (Fig. S21, ESI[†]). Furthermore, as shown in X-ray diffraction (XRD) patterns in Fig. S22 (ESI[†]), the characterized peaks for NCM111 cathode completely disappeared after cycling in P-DOL PE, while no obvious change was observed for the NCM111 cathode after cycling in P-DOX PE, suggesting that a stable bulk structure was preserved. In addition, according to the XPS results (Fig. S23, ESI[†]), much fewer decomposition byproducts were detected on NCM111 cathode after cycling in P-DOX PE compared to that cycling in P-DOL PE, which was attributed to the superior oxidation stability of the P-DOX that inhibits the continuously parasitic reaction between the cathode and the PE. Furthermore, as shown in Fig. 6d and Fig. S24 (ESI[†]), the $\text{Li}||\text{NCM111}$ cell using P-DOX PE also exhibits excellent rate capability from 0.1C to 5C, with a specific capacity of $158.2 \text{ mA h g}^{-1}$ at 0.1C and can maintain a high capacity of $110.1 \text{ mA h g}^{-1}$ at 5.0C, which is sufficient for its practical application at room temperature.

As the energy density is proportional to the capacity and discharge voltage of the cell, elevating the upper cutoff voltage of the cell would greatly boost its energy density. Therefore, the superiority of this *in situ* formed P-DOX PE was further investigated under higher cutoff voltages. As shown in Fig. S25 (ESI[†]), under a cutoff voltage of 4.4 V, the $\text{Li}||\text{NCM111}$ cell still exhibits excellent cycling stability with a high-capacity retention of 96.0% after 300 cycles at 1.0C. When the cutoff voltage was further raised to 4.5 V, the initial capacity increases to $161.6 \text{ mA h g}^{-1}$, and its capacity retention is also as high as of 96.0% after 100 cycles at 1.0C (Fig. 7a). Moreover, the charge–discharge profiles remain very stable with extremely low polarization voltage, demonstrating excellent oxidation stability of the P-DOX PE under high-voltage.

To further investigate the universality of this *in situ* polymerized P-DOX PE, $\text{Li}||\text{NCM811}$ and $\text{Li}||\text{LCO}$ full cells were also

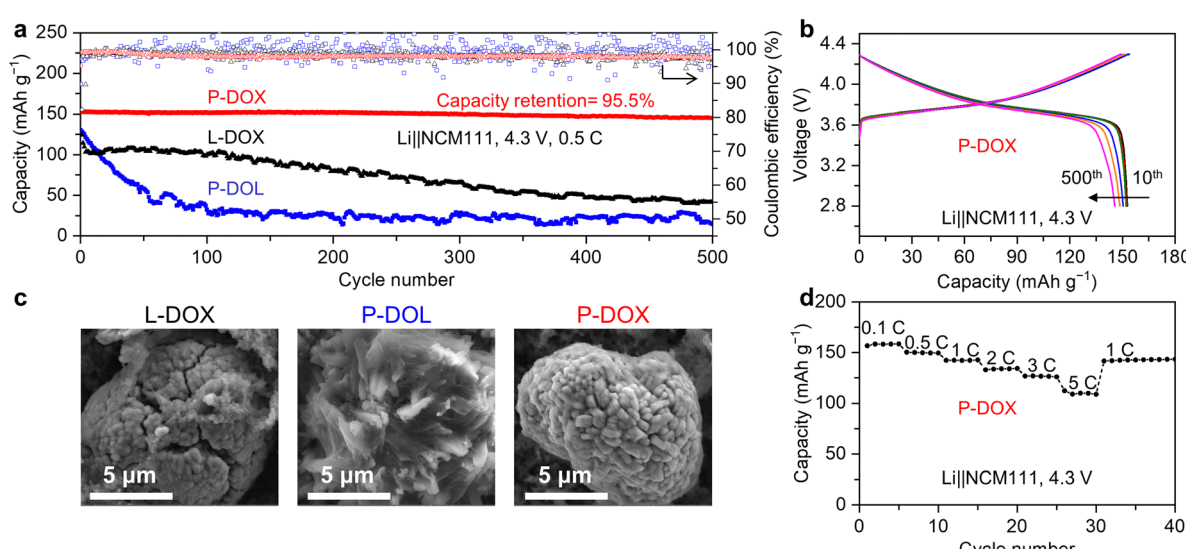


Fig. 6 Electrochemical performance of the Li-metal full-cells at 4.3 V. (a) Cycling performance of the $\text{Li}||\text{NCM111}$ full-cells using various electrolytes. (b) Selected charge–discharge profiles of the $\text{Li}||\text{NCM111}$ full-cell using P-DOX PE. (c) SEM images of the NCM111 cathodes after 500 cycles in $\text{Li}||\text{NCM111}$ cells. (d) Rate performance of the $\text{Li}||\text{NCM111}$ full-cell using P-DOX PE. The tests were conducted within a cutoff voltage of 2.8–4.3 V at 0.5C.

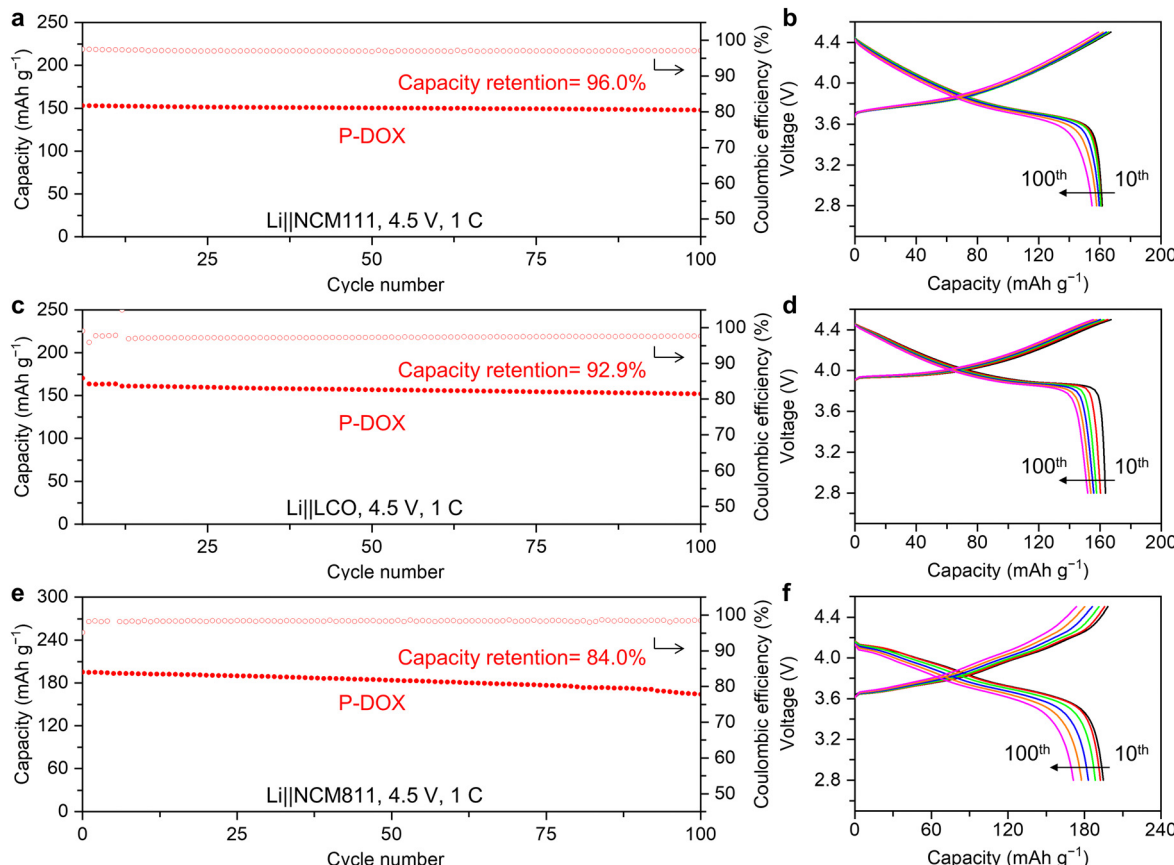


Fig. 7 Electrochemical performance of the Li-metal full-cells at 4.5 V. (a) Cycling performance and (b) selected charge–discharge profiles of the Li||NCM111 full-cell. (c) Cycling performance and (d) selected charge–discharge profiles of the Li||LCO full-cell. (e) Cycling performance and (f) selected charge–discharge profiles of the Li||NCM811 full-cell. The tests were conducted within a cutoff voltage of 2.8–4.5 V at 1.0C.

assembled and subjected to the test under a high cutoff voltage of 4.5 V. As shown in Fig. 7, the Li||LCO cell delivers a high initial capacity of 163.5 mA h g⁻¹ and an excellent capacity retention of 92.9% after 100 cycles at 1.0C. Meanwhile, the Li||NCM811 cell exhibits a high capacity of 195.3 mA h g⁻¹ with more than 84.0% capacity retained after 100 cycles at 1.0C, which breaks the voltage limitation for conventional polyether-based PE and represents the pioneering report in solid-state LMBs under such a high voltage (Table S2, ESI†). The above experimental results indicate that the *in situ* polymerized P-DOX PE has good universality for various state-of-the-art high-voltage cathodes, together with the same process as commercial battery assembly and manufacturing, it holds great prospects for commercialization and practical application.

Conclusions

In summary, we herein report the *in situ* polymerization of 1,3-dioxane (DOX) for application as a polymer electrolyte (PE) for high-voltage Li-metal batteries (LMBs). It is demonstrated that the resulting poly(DOX) PE exhibits superior oxidation stability (>4.7 V) owing to its prolonged alky chain that lowers its HOMO level, and excellent Li compatibility owing to its weak solvating ability that leads to a highly robust inorganic-rich SEI.

Consequently, the *in situ* formed poly(DOX) PE enables highly dense and smooth Li deposition morphology as well as excellent reversibility in Li plating/stripping cycling for over 1300 h. As a result, this *in situ* fabricated poly(DOX) PE markedly improves the cycling stability of Li||NCM111, Li||NCM811 and Li||LCO full cells under a high cut-off voltage of 4.5 V. Therefore, this work demonstrates the effectiveness of tuning the molecular structure of the monomer in improving the high-voltage tolerance and metal-anode compatibility of the resulting *in situ* polymerized PEs, which represents a significant advancement in the design of PEs for high-energy-density solid-state batteries.

Experimental section

Electrolyte preparation

Electrolyte preparation was conducted in an argon-filled glove box, in which both the O₂ and H₂O contents were maintained below 0.01 ppm. The L-DOX electrolyte was prepared by dissolving lithium bis(fluorosulfonyl)imide (LiFSI) salt in 1,3-dioxane (DOX) at a molar ratio of 1 : 8 (corresponding to 1.47 M). For the preparation of P-DOX PE, 20 mmol Al(OTf)₃ was added to 1 mL of the L-DOX electrolyte, then was heated at 60 °C for 36 h.

The P-DOL PE was prepared under the similar conditions except that the polymerization time was controlled at 12 h.

Electrode preparation

The NCM111 cathode slurry was prepared by mixing NCM111 powder, acetylene black, and poly(vinylidene fluoride) (PVDF) at a weight ratio of 80:12:8 in *N*-methyl-2-pyrrolidone (NMP). Then, the slurry was coated on aluminum foil and dried in a vacuum oven at 100 °C for 24 h. The active mass loading of NCM111 cathode was about 2.5–3.0 mg cm⁻². The LCO and NCM811 cathodes were prepared using a similar procedure with the active mass loading controlled at about 2.5–3.0 mg cm⁻².

Material characterization

GPC measurements were performed by dissolving the P-DOL and P-DOX PEs in THF, and then the solution was eluted in a Waters ambient temperature GPC equipped with a triple detection function for absolute polymer molecular weight determination (Agilent waters1515). The molecular weight calibration was performed using a polymethyl methacrylate (PMMA) standard sample. The P-DOL and P-DOX PEs were dissolved in dimethyl sulfoxide-d₆ for ¹H NMR measurements. For ⁷Li NMR analysis, the PE was *in situ* polymerized inside a coaxial NMR tube. A capillary filled with a solution containing 1 mg LiCl dissolved in 0.5 mL D₂O was used as an internal reference. The NMR spectra were recorded using a 600 MHz NMR spectrometer (Bruker AVANCE NEO).

FTIR spectra of the electrolytes were characterized by an IR Prestige-21 spectrometer (Japan Shimadzu). The chemical composition on the surface of the electrode was analyzed by XPS (PerkinElmer PHI 1600 ESCA). The Raman spectrum of the electrolyte was obtained using a QE Pro spectrometer (Ocean Optics) with an emission wavelength of 532 nm. The X-ray powder diffraction patterns were collected using a diffractometer (D8 Advance, Bruker) with Cu K α radiation. The DSC was tested using a TA-60WS Differential Scanning Calorimeter (Japan Shimadzu, TA-60WS). The TGA tests was conducted using a TG 209 (METZSCH, F1 Libra). The morphology was investigated using a scanning electron microscopy (SEM, MAIA3, TESCAN Brno, s.r.o.). In operando observation of lithium deposition was performed using an optical microscope (Yuescope, YM710TR). The flammability of the electrolytes was tests by burning an electrolyte-infiltrated glass fiber separator.

The GPC and NMR characterization studies were conducted with both *in situ* and *ex situ* generated PEs to better reflect the actual situation in the cells. Since a large amount of testing sample is required, the other characterization studies were performed with the *ex situ* generated PEs.

Electrochemical measurements

Using an argon-filled glove box, all cells were assembled in a standard 2032-type coin-cell using Li foil as the anode and Celgard 3501 as the separator. The separator was used to provide separation and control the thickness of the *in situ* polymerized PEs, which can avoid short circuits in the liquid state. The amount of the liquid electrolyte employed was 80 μ L

for each cell during cell assembly. The cells were placed in an oven at 60 °C for 36 h before testing to complete the polymerization. The thickness of the *in situ* generated PEs (*i.e.*, polymer-infiltrated separators) was measured at ~30 μ m. The electrochemical tests were conducted at room temperature unless otherwise stated. The galvanostatic charge–discharge tests for Li||Li, Li||NCM111, Li||NCM811, and Li||LCO cells were carried out using a CT2001A charge–discharge tester (Wuhan Land, China) at different current densities.

The linear sweep voltammetry (LSV), Li⁺ transference number, electrochemical floating, and electrochemical impedance spectroscopy (EIS) tests were conducted using a VMP3 potentiostat (Bio-Logic). The LSV test was performed in a two-electrode system at a scanning rate of 1 mV s⁻¹. The EIS was tested at the frequency range of 0.1–10⁶ Hz with an amplitude of 10 mV. The electrochemical floating test was conducted in a Li||NCM111 cell, which was first charged to 4.0 V, then held at progressively higher voltage, each for 5 h. The critical current density (CCD) test was performed in a Li||Li symmetric cell, which was charged at the constant current density increases by 0.5 mA cm⁻² per cycle starting from 0.5 mA cm⁻², each cycle for 1 h.

Data availability

All the data supporting the findings of this study are available within the article and its ESI.† Additional data related to this article can be obtained from the corresponding author upon reasonable request.

Author contributions

Q. Z. conceived the idea and directed the project. K. D. and Y. L. proposed and designed the experiments. Y. L. and H. Z. prepared the polymer electrolytes and electrodes, performed electrochemical measurements and battery tests, collected GPC and NMR spectra. Z. H. measured DSC and TGA data. Q. W. performed XPS and FTIR measurements. J. Lai took the SEM images. Y. Z. performed the *in situ* operando observation of the Li deposition. J. Li performed the theoretical calculations. J. W. performed the Raman measurement. Y. L. wrote the manuscript, and Q. Z., K. D. and Y.-Q. L. edited the manuscript. All authors contributed to the discussion.

Conflicts of interest

The authors declare no competing interests.

Acknowledgements

This work was supported by the National Natural Science Foundation of China (no. 22005108 and 22209050), and the Natural Science Foundation of Guangdong Province (no. 2021A1515110397, 2022B1515020005, and 2023A1515012032).

References

- 1 J. W. Choi and D. Aurbach, *Nat. Rev. Mater.*, 2016, **1**, 1–16.
- 2 Z. Cheng, T. Liu, B. Zhao, F. Shen, H. Jin and X. Han, *Energy Storage Mater.*, 2021, **34**, 388–416.
- 3 M. Du, Y. Sun, B. Liu, B. Chen, K. Liao, R. Ran, R. Cai, W. Zhou and Z. Shao, *Adv. Funct. Mater.*, 2021, **31**, 2101556.
- 4 C. Guo, Y. Shen, P. Mao, K. Liao, M. Du, R. Ran, W. Zhou and Z. Shao, *Adv. Funct. Mater.*, 2022, **33**, 2213443.
- 5 W. Li, B. Song and A. Manthiram, *Chem. Soc. Rev.*, 2017, **46**, 3006–3059.
- 6 B. Liu, J.-G. Zhang and W. Xu, *Joule*, 2018, **2**, 833–845.
- 7 J. Lai, Y. Huang, X. Zeng, T. Zhou, Z. Peng, Z. Li, X. Zhang, K. Ding, C. Xu, Y. Ying, Y.-P. Cai, R. Shang, J. Zhao and Q. Zheng, *ACS Energy Lett.*, 2023, **8**, 2241–2251.
- 8 J. Shi, C. Xu, J. Lai, Z. Li, Y. Zhang, Y. Liu, K. Ding, Y. P. Cai, R. Shang and Q. Zheng, *Angew. Chem., Int. Ed.*, 2023, **62**, 202218151.
- 9 K. Xu, *J. Power Sources*, 2023, **559**, 232652.
- 10 S. Wei, S. Choudhury, Z. Tu, K. Zhang and L. A. Archer, *Acc. Chem. Res.*, 2018, **51**, 80–88.
- 11 K. Liu, Y. Liu, D. Lin, A. Pei and Y. Cui, *Sci. Adv.*, 2018, **4**, aas9820.
- 12 Y. Zhou, K. Zhao, Y. Han, Z. Sun, H. Zhang, L. Xu, Y. Ma and Y. Chen, *J. Mater. Chem. A*, 2019, **7**, 5712–5718.
- 13 S. Zhang, S. Li and Y. Lu, *eScience*, 2021, **1**, 163–177.
- 14 M. A. Cabañero Martínez, N. Boaretto, A. J. Naylor, F. Alcaide, G. D. Salian, F. Palombarini, E. Ayerbe, M. Borras and M. Casas-Cabanas, *Adv. Energy Mater.*, 2022, **12**, 2201264.
- 15 L. Han, L. Wang, Z. Chen, Y. Kan, Y. Hu, H. Zhang and X. He, *Adv. Funct. Mater.*, 2023, **33**, 2300892.
- 16 A. Manthiram, X. Yu and S. Wang, *Nat. Rev. Mater.*, 2017, **2**, 1–16.
- 17 J. Janek and W. G. Zeier, *Nat. Energy*, 2023, **8**, 230–240.
- 18 F. Q. Liu, W. P. Wang, Y. X. Yin, S. F. Zhang, J. L. Shi, L. Wang, X. D. Zhang, Y. Zheng, J. J. Zhou, L. Li and Y. G. Guo, *Sci. Adv.*, 2018, **4**, aat5383.
- 19 Q. Zhao, X. Liu, S. Stalin, K. Khan and L. A. Archer, *Nat. Energy*, 2019, **4**, 365–373.
- 20 Y. G. Cho, C. Hwang, D. S. Cheong, Y. S. Kim and H. K. Song, *Adv. Mater.*, 2019, **31**, 1804909.
- 21 T. Liu, J. Zhang, W. Han, J. Zhang, G. Ding, S. Dong and G. Cui, *J. Electrochem. Soc.*, 2020, **167**, 070527.
- 22 S.-J. Tan, J. Yue, Y.-F. Tian, Q. Ma, J. Wan, Y. Xiao, J. Zhang, Y.-X. Yin, R. Wen, S. Xin and Y.-G. Guo, *Energy Storage Mater.*, 2021, **39**, 186–193.
- 23 J. Zhu, J. Zhang, R. Zhao, Y. Zhao, J. Liu, N. Xu, X. Wan, C. Li, Y. Ma, H. Zhang and Y. Chen, *Energy Storage Mater.*, 2023, **57**, 92–101.
- 24 G. Xu, A. Kushima, J. Yuan, H. Dou, W. Xue, X. Zhang, X. Yan and J. Li, *Energy Environ. Sci.*, 2017, **10**, 2544–2551.
- 25 S. Huang, Z. Cui, L. Qiao, G. Xu, J. Zhang, K. Tang, X. Liu, Q. Wang, X. Zhou, B. Zhang and G. Cui, *Electrochim. Acta*, 2019, **299**, 820–827.
- 26 J. Xiang, Y. Zhang, B. Zhang, L. Yuan, X. Liu, Z. Cheng, Y. Yang, X. Zhang, Z. Li, Y. Shen, J. Jiang and Y. Huang, *Energy Environ. Sci.*, 2021, **14**, 3510–3521.
- 27 J. Yu, X. Lin, J. Liu, J. T. T. Yu, M. J. Robson, G. Zhou, H. M. Law, H. Wang, B. Z. Tang and F. Ciucci, *Adv. Energy Mater.*, 2021, **12**, 2102932.
- 28 A. Hu, Z. Liao, J. Huang, Y. Zhang, Q. Yang, Z. Zhang, L. Yang and S.-I. Hirano, *Chem. Eng. J.*, 2022, **448**, 137661.
- 29 S. Wen, C. Luo, Q. Wang, Z. Wei, Y. Zeng, Y. Jiang, G. Zhang, H. Xu, J. Wang, C. Wang, J. Chang and Y. Deng, *Energy Storage Mater.*, 2022, **47**, 453–461.
- 30 Q. Ma, J. Yue, M. Fan, S. J. Tan, J. Zhang, W. P. Wang, Y. Liu, Y. F. Tian, Q. Xu, Y. X. Yin, Y. You, A. Luo, S. Xin, X. W. Wu and Y. G. Guo, *Angew. Chem., Int. Ed.*, 2021, **60**, 16554–16560.
- 31 Z. Geng, Y. Huang, G. Sun, R. Chen, W. Cao, J. Zheng and H. Li, *Nano Energy*, 2022, **91**, 106679.
- 32 Y. Du, L. Zhao, C. Xiong, Z. Sun, S. Liu, C. Li, S. Hao, W. Zhou and H. Li, *Energy Storage Mater.*, 2023, **56**, 310–318.
- 33 W. H. Meyer, *Adv. Mater.*, 1998, **10**, 439–448.
- 34 Y. Chen, Z. Yu, P. Rudnicki, H. Gong, Z. Huang, S. C. Kim, J.-C. Lai, X. Kong, J. Qin, Y. Cui and Z. Bao, *J. Am. Chem. Soc.*, 2021, **143**, 18703–18713.
- 35 K. Dokko, D. Watanabe, Y. Ugata, M. L. Thomas, S. Tsuzuki, W. Shinoda, K. Hashimoto, K. Ueno, Y. Umebayashi and M. Watanabe, *J. Phys. Chem. B*, 2018, **122**, 10736–10745.
- 36 Y. Yamada, K. Furukawa, K. Sodeyama, K. Kikuchi, M. Yaegashi, Y. Tateyama and A. Yamada, *J. Am. Chem. Soc.*, 2014, **136**, 5039–5046.
- 37 H. Yang, B. Zhang, M. Jing, X. Shen, L. Wang, H. Xu, X. Yan and X. He, *Adv. Energy Mater.*, 2022, **12**, 2201762.
- 38 J. Tan, J. Matz, P. Dong, J. Shen and M. Ye, *Adv. Energy Mater.*, 2021, **11**, 2100046.